Chapter 2
Experimental Setup and Background

The experimental task of this thesis is to prepare magnetic and non-magnetic bulk impurities and to investigate these systems by scanning tunneling microscopy (STM). In the first part of this chapter the sample preparation will be described. The main experimental instrumentation, the low temperature STM as well as the standard theory for the interpretation are introduced in the second part.

2.1 Sample Preparation

The basic idea of preparing single sub-surface atoms is very simple. Starting with a clean Cu(100) single crystal a thin alloy containing the host and the impurity material is epitaxially grown onto the substrate by using two electron beam evaporators. In order to get a well-defined sample system, the preparation has to meet several requirements. For the investigation of single atoms a low concentration of impurities is sufficient. Therefore, the host evaporator operates at moderate rates (1–2 ML/min, monolayer per minute), whereas the second one is kept at very low deposition rates (0.1 ML/min). To avoid unwanted contamination the whole preparation is performed under ultra-high vacuum (UHV) conditions ($p < 10^{-9}$ mbar) using high purity materials and a carefully cleaned substrate. Furthermore, the resulting surface should provide large atomically flat areas to get a well-defined tunneling geometry.

2.1.1 UHV Preparation Chamber

The sample preparation is carried out in a mobile UHV-chamber. In combination with a valve and a turbo-molecular pump this chamber allows an immediate transfer of the sample to various existing UHV-chambers for example the

STM-chamber or the characterization chamber without breaking the vacuum. After 48 h bake-out at 150 °C a base pressure of $p < 5 \times 10^{-11}$ mbar is achieved.

For the sample preparation the chamber is equipped with three independent operating electron beam evaporators, an ion sputtering system and a pyrometer for non-contact temperature measurement. The sample is mounted below a liquid nitrogen (LN_2) tank which allows cooling of the sample. Using a tungsten filament the sample can be heated from the back side of the crystal. With this setup substrate temperatures from 100 K up to 1,300 K can be achieved. Additionally, the sample holder possesses six electrical contacts (multi-segment sample holder). The electrical contact is necessary to apply a high voltage to the sample in order to perform electron beam heating and to suppress ion bombardment during evaporation. Furthermore, the electrical contact is used to ground the sample during sputtering. The current directly gives rise to the amount of argon ions hitting the sample per second. A detailed description of the sample preparation chamber can be found in [1, 2].

2.1.2 Single Crystal Preparation and Characterization

As substrate material a single crystal of copper is used in this work, which is commercially available from MaTeck, Jülich. The crystal is 1 mm thick and has a hat-like shape with diameters of 8.5 mm and 6.0 mm, respectively. The surface is oriented normal to the [100] direction with an accuracy better than 0.1 % and is polished to a roughness smaller than 30 nm. According to the specification the purity is better than 99.9999 %.

In order to get a well-defined epitaxial growth of the copper alloy one needs a clean and atomically flat substrate. In case of the Cu(100) single crystal substrate this goal can be achieved by cycles of argon ion bombardment at room temperature followed by electron beam heating. Typically ten cycles are enough to achieve a clean surface. The ion bombardment leads to sputtering of the surface as well as to argon implantation in the surface region. Both effects lead to a distorted crystalline structure at the surface. The crystalline structure is recovered by a short annealing step. The temperature must be high enough or the duration long enough that all implanted argon atoms diffuse to the surface and leave the sample. Moreover, during the annealing bulk defects segregate towards the surface. They are removed in subsequent sputtering steps. In the following a detailed description of the methods for the Cu(100) single crystal preparation will be given.

2.1.3 Sample Holder

The sample holder has to fulfill several requirements: on the one hand a good thermal contact to the cryostat is essential. On the other hand to heat only the
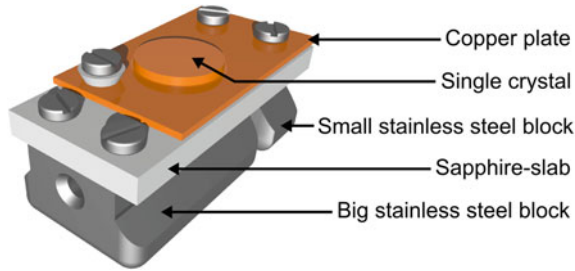
Fig. 2.1 Design of the low temperature sample holder. The Cu(100) crystal is fixed onto the sapphire slab by a copper plate. An electrical contact to the crystal is provided by the backward small stainless steel block

crystal and not the whole sample holder an electrical insulation is necessary for the application of electron beam heating. To meet these requirements the sample holder consists of two different sized dovetail-shaped blocks made of stainless steel. The blocks are hold together by a sapphire-slab on which the copper crystal is placed. Sapphire is an electrical insulating material which has a high thermal conductivity. To beware of contamination by secondary sputtering effects the single crystal of copper is pressed with caution onto the sapphire-slab by a copper plate or copper-covered molybdenum plate. The complete design of the sample holder is sketched in Fig. 2.1.

The crystal can be electrically contacted by the small stainless steel block. A hole in both, the big block and the sapphire-slab gives access to the back side of the crystal. For the electron beam heating process a tungsten wire can be inserted in this opening. The geometry of the sample holder and the hat-like shape of the crystal avoid direct trajectories between sample holder and the crystal surface. Therefore, a contamination by secondary processes during argon sputtering is suppressed.

2.1.4 Argon Sputtering

For removing surface material a sputtering source (IQE11/35 by SPECS, Berlin) is used. The general concept of sputtering can be summarized as follows: Argon atoms, entering the preparation chamber through a variable leak valve, are ionized by an electron beam and accelerated to the sample by a high voltage. By tuning the pressure in the chamber and by measuring the ion flux on the sample the intensity of the argon ion beam is adjustable. Typical values for the current densities are $0.81–2 \times 10^{-2} \, A \, m^{-2}$ with 700 eV ion beam energy. At the beginning of the preparation the sputtering goes on for one hour to remove the oxide film and structures coming from prior experiments. After the sample is sputtered for one hour, the sputtering time is reduced to 20 min for all following cleaning cycles.

2.1.5 Annealing

The sample heating is realized by electron bombardment. A tungsten wire is brought into close contact to the backside of the crystal using a z-micrometer drive. Filament currents in the order of 5–7 A lead to a thermal emission of electrons that are accelerated to the crystal by applying a positive voltage to the sample. This setup allows powers up to 50 W resulting in temperatures up to 1,300 K. The temperature can be monitored by a pyrometer (IM120 by IMPAC, Frankfurt) in the range from 430 K to 1,570 K. For the emissivity of the clean Cu(100) surface a value of 11 % is proposed [1]. During the annealing process the crystal is heated up by a rate of approximately 50 K/min to a final temperature of 700 K. When the temperature is reached, it is kept constant for 10 min followed by a step by step cool down extended over 10 min. For the last cycle, before starting the thin film epitaxy the annealing time is reduced to 5 min to avoid segregation of bulk defects.

2.1.6 Substrate Characterization

The single crystal preparation procedure is tested by the non-local surface sensitive methods low energy electron diffraction (LEED) and Auger electron spectroscopy (AES). These two methods allow investigating the crystalline quality of the sample and the chemical composition of the surface after the preparation, respectively.

In Fig. 2.2a the AES spectrum before the cleaning procedure is shown. By comparing the signature with reference spectra [3] one observes that besides copper (Cu) also oxygen (O), carbon (C) and molybdenum are present at the beginning of the sample preparation. After three cycles of sputtering and heating the oxygen and the carbon signature decreases while the intensity of the copper peaks increases. Finally, after nine cycles no signature of carbon and oxygen is observed. This shows that the cleaning procedure works very well resulting in a defect free surface. Only peaks referred to molybdenum and copper are found in the spectrum. The peaks belonging to molybdenum are due to defocussing of the electron beam which hits not only the crystal but also the sample holder.

The crystalline quality is analyzed by the LEED diffraction pattern, see Fig. 2.2b. It shows sharp peaks resembling the diffraction characteristics of an fcc-crystal structure. The high quality of the cleaned Cu(100) substrate is confirmed by a high resolution STM topography (see Fig. 2.2c) revealing large and homogeneous terraces, which are separated by atomic steps.

2.1.7 Epitaxy of Diluted Cu Films

To get well-defined alloys only high purity materials are used in this work. The materials were purchased from Alfa Aesar and have a purity of 99.995 % (Co, Fe),
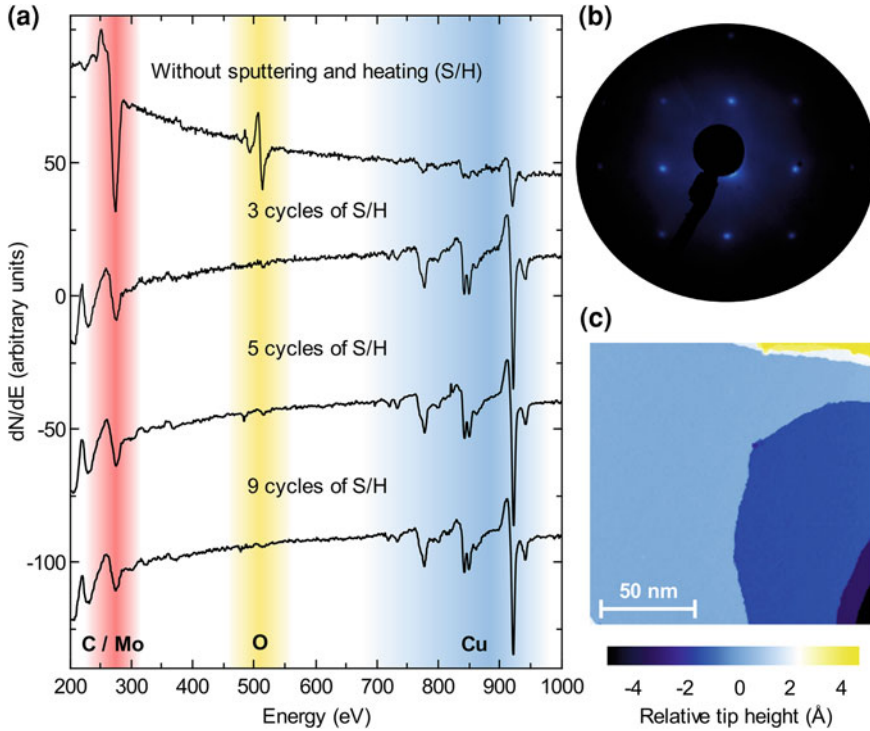
Fig. 2.2 Characterization of the prepared Cu(100) surface. **a** AES spectra (*shifted vertically for clarity*) before and after several cycles (3, 5, 9) of sputtering and heating. Characteristic energy intervals for the atomic species C, O and Cu are highlighted by color. **b** After the cleaning procedure the LEED diffraction pattern taken at 170 eV reveals sharp peaks. **c** In the STM topography (150 nm × 150 nm, 1 V, 50 pA) a flat surface is observed which offers large and defect free terraces

99.9999 % (Ag) and 99.9999 % (Cu). Before the deposition, the evaporators are outgassed for roughly 2 h. This means that they are kept at high flux rates (compared to the actual thin film epitaxy) until the pressure in the preparation chamber is constant.

After manufacturing a clean and flat Cu(100) surface, thin films of diluted copper are deposited onto the clean substrate. Therefore, electron beam evaporators (e-beam by TECTRA, Frankfurt) are used. Electrons which are emitted by a tungsten filament are accelerated due to high voltage to the material to be evaporated. The evaporant, which is either a rod (Co and Fe) or located in a tungsten crucible (Cu and Ag), is heated up and goes into the gas phase. A small percentage of these vapor-phase atoms are ionized by the electron beam. A fraction of the ionized atoms can be captured and used to control the material flux. A detailed description of the evaporators, their functionality as well as their close-loop control is given in [1, 2, 4–6]. In the following only the most important facts and parameters for the preparation of Ag-, Co- and Fe-diluted copper films will be discussed.

It turned out that for the deposition of copper one has to take care of positively charged atoms. Although they are useful for the control of the flux they are repelled by the crucible and directly accelerated to the sample. The ion flux, measured directly at the sample using a deposition rate of 1 ML/min is 0.4×10^{-2} A m^{-2}. This value and the energy of the ions (800–1,400 eV) are comparable to the argon bombardment used for cleaning the crystal. As a result, the ionized atoms have an impact on the morphology and the growth process for thin copper films. A detailed study of the influence of sputtering during growth of copper on Cu(100) can be found in [6]. To avoid the sputtering effect a high positive voltage (800–1,400 V) is applied to the crystal during the evaporation.

In order to investigate single individual isolated impurity atoms one has to be able to prepare alloys which contain only low defect concentrations of less than 0.1 %. One possibility is to use very low deposition rates for the impurity material. The lowest stable rates which can be realized for iron, cobalt and silver are of the order of 0.1 ML/min. To achieve impurity concentration of less than 0.1 %, this implies a copper deposition rate of more than 100 ML/min. These high rates cannot be reached for the electron beam evaporation of copper. To obtain low concentrations for moderate copper flux rates computer controlled stepper motors are attached to the shutter of the evaporator containing the impurity material. The stepper motors provides shutter opening times down to 50 ms. Using this setup the deposition of thin copper films with low defect concentrations down to 0.01 % is possible by using moderate copper fluencies of about 0.5–1 ML/min. In the following the preparation of Co-, Fe- and Ag-diluted copper films is described in detail.

2.1.8 Co in Cu(100)

After the cleaning procedure six monolayers of copper were deposited onto the substrate using a deposition rate of 1 ML/min. In a next step, under continuous copper deposition the cobalt shutter is opened for 100 ms every minute for 12 min. At the same time, the deposition rate for Co is stabilized at 0.13 ML/min. This value theoretically corresponds to a cobalt concentration of $c_{Co} = 0.02$ % and is in good agreement to the concentration that is observed in the experiment [6]. Finally, two layers of pure copper are deposited. The whole epitaxy is carried out at a substrate temperature[1] $T_S = 420$ K to ensure a layer by layer growth resulting in a very flat surface [6].

---

[1] According to calibration measurements, a constant heating power of 3 W corresponds to a sample temperature of $T_S = 420$ K.

2.1.9 Fe in Cu(100)

First attempts trying the same recipe for the preparation of iron doped copper films result in a high number of iron clusters located in the surface layer. Nearly all Fe atoms segregate to the surface layer for the same growth conditions as for Co ($T_S = 420\,$K). A way to reduce the mobility of the iron atoms during epitaxy is to go to lower temperatures. Therefore, the substrate is cooled down to 100 K prior to deposition. After doing this, nine monolayers of copper are evaporated using a deposition rate of 0.5 ML/min. Then for 18 min every 2 min the iron shutter is opened for 160 ms. The deposition rate is well stabilized at 0.2 ML/min. Finally, two monolayers of copper were deposited on top. The low temperature growth hinders the iron atoms to segregate to the surface but has the drawback of producing a very rough surface not suitable for an STM experiment. To overcome this shortcoming, the sample is flushed to a temperature of 470 K for 5 s. After this the electron beam heating is rapidly ceased. The short annealing step is sufficient for surface diffusion of copper atoms and results in a flat surface with $50\,$nm $\times$ $50\,$nm atomic step free terraces. Although the concentration of the iron atoms embedded in the copper crystal should be in principle the same as in the cobalt case described above, only a fraction of the concentration of the impurities is located below the surface. There are still iron clusters in the first atomic layer of the surface indicating that there is still room for sample preparation improvements.

2.1.10 Ag in Cu(100)

The silver-doped copper film is prepared in the same manner using a low temperature deposition. After eight monolayers of copper are deposited at 1 ML/min, ten monolayers of a 0.02 % silver-copper alloy are grown. Then, two layers of copper are grown on top. Finally, the sample is annealed to 470 K followed by a fast cool down procedure.

2.2 Scanning Tunneling Microscopy

The scanning tunneling microscope (STM) was invented by G. Binnig and H. Rohrer in 1982 at the IBM research center in Zürich [7, 8]. It is based on the concept of tunneling. This quantum effect causes a current flow between a metal tip and a conductive sample if they are brought into close proximity to each other with a bias voltage applied simultaneously. For a given tip-sample system the resulting tunneling current is a function of the applied bias voltage, the tip-sample distance and the lateral tip position. Keeping the bias voltage and the lateral tip position fixed, the tunnel current depends exponentially on the tip-sample distance.

This fact can be utilized to stabilize the tip height by using a close-loop control and piezoelectric elements. Local information about the sample is gained by scanning the tip across the surface (x, y).

Since the tip is separated only a few angstroms from the surface, the STM technique requires excellent damping of internal (liquid nitrogen and helium) and external (building and noise) vibrational sources. Moreover, clean surfaces, stable and sharp tips and good electronic equipment are necessary for high quality STM measurements. An introduction to scanning tunneling microscopy and related techniques can be found in [9–11].

The experiments in this thesis were performed using a home built low temperature STM operating at pressures below $p < 5 \times 10^{-11}$ mbar. The scanning unit is a Besocke-type piezo-unit [12] mounted on the bottom of a liquid helium (LHe) bath cryostat. The scanner and the sample support are thermally coupled to the helium bath via sapphire plates and indium foils. Small silver wires interconnect the tip and the cryostat. A liquid nitrogen (LN_2) vessel surrounds the LHe-tank and STM-head shielding the heat radiation. An optical access is provided by windows in the nitrogen cup. These openings are covered by special glasses that absorb infrared radiation. This setup provides a sample and tip cooling and the possibility replacing both of them in-situ. The sample temperature is estimated around 6 K. Recent scanning tunneling potentiometry studies investigating the thermovoltage between tip and sample indicate that the temperature of the tip is slightly higher than 6 K [13]. Measurements considering the Cu(100) surface reveal an thermovoltage signal—the experimentally uncertainty of the applies bias voltage—with amplitude up to 0.3 mV. This value is small compared to the voltage ranges considered in this work and hence the thermovoltage is neglected in the following.

2.2.1 Standard STM Theory

There exists no complete theoretical formalism describing the tunneling process in all its diversity. The most widely used models start with a tunneling formalism proposed by Bardeen calculating the current from the sample and tip states of the unperturbed systems using first order perturbation theory [14]. Transition of electrons can only take place from filled sample states φ_v^S into empty tip states φ_μ^T or from filled tip states into empty sample states. Applying a voltage V to the sample, the tunneling current $I(V)$ can be expressed as

$$I(V) = \frac{4\pi e}{\hbar} \sum_{v,\mu} \left[f\left(E_\mu^T - E_F^T\right) - f\left(E_v^S - E_F^S\right) \right] |M_{v,\mu}|^2 \delta\left(E_v^S - E_\mu^T - eV\right) \quad (2.1)$$

where $f(\varepsilon) = (1 + \exp(\varepsilon/k_B T))^{-1}$ is the Fermi-Dirac distribution and $M_{v,\mu}$ is the tunneling matrix element describing the transition probability from state φ_v^S to state φ_μ^T. The Dirac delta function restricts the tunneling process to states fulfilling

energy conservation. Under the assumption that the tunneling matrix element $M_{\nu,\mu}$ does only depend on the energetic position of the considered states, the summation of the states in Eq. (2.1) can be replaced by an integration over the density of states (DOS) of tip ρ^T and sample ρ^S.

$$
\begin{aligned}
I(V) = \frac{4\pi e}{\hbar} \int d\varepsilon \big[f\big(E_F^S - eV + \varepsilon\big) - f\big(E_F^T + \varepsilon\big) \big] \\
\times \rho^S\big(E_F^S - eV + \varepsilon\big) \rho^T\big(E_F^T + \varepsilon\big) \big| M\big(E_F^S - eV + \varepsilon, E_F^T + \varepsilon\big) \big|^2
\end{aligned}
\tag{2.2}
$$

This formula links the tunneling current to the electronic properties of tip and sample described by the density of states. The distance dependence as well as the lateral dependence of the current are included in the matrix element M. For low temperature the Fermi-Dirac distribution can be approximated by a step function.

$$
I(V) = \frac{4\pi e}{\hbar} \int\limits_0^{eV} d\varepsilon \rho^S\big(E_F^S - eV + \varepsilon\big) \rho^T\big(E_F^T + \varepsilon\big) |M|^2
\tag{2.3}
$$

Assuming further small voltages V the integral can be simplified. The tunnel current then reads

$$
I(V) = \frac{4\pi e^2}{\hbar} V \rho^S\big(E_F^S\big) \rho^T\big(E_F^T\big) \big| M\big(E_F^S, E_F^T\big) \big|^2
\tag{2.4}
$$

The model so far for the tunneling current is a consequence of Bardeen's tunneling formalism connecting the current to a transfer matrix element. In a next step, it is necessary to calculate this element for the special geometry of a sharp tip in front of a sample. In general, the shape and the electronic structure of the tip are unknown in the experiment. Tersoff and Hamann approximated the tip as an s-like wave function centered at the tip apex $\vec{r}^T$. They relate the tunnel current to the local density of states of the sample at the position of the tip [15, 16].

$$
I(V) \propto V \rho^T(\varepsilon) \rho^S\big(\varepsilon, \vec{r}^T\big)
\tag{2.5}
$$

According to Tersoff and Hamann the tunneling current is proportional to the applied voltage, the tip density of states and the sample density of states at the tip position.

For STM measurements at higher voltages the above assumption of a constant energy-independent transfer matrix element is no longer valid. The matrix element changes for states of different energies. A complete energy-dependent description of this problem is rather complicated. A simplified model by Hamer's replaces the tunneling matrix element $|M|^2 \rightarrow T(\varepsilon, eV, z)$ by a transition probability $T(\varepsilon, eV, z)$ [17]. The current is then obtained by an integration of all possible energies where tunneling can occur.

$$I(V, x, y) = \frac{4\pi e}{\hbar} \int\limits_0^{eV} d\varepsilon \rho^S \left(E_F^S - eV + \varepsilon, x, y\right) \rho^T \left(E_F^T + \varepsilon\right) T(\varepsilon, eV, z) \qquad (2.6)$$

The transmission probability is calculated using the Wentzel-Kramers-Brillouin approximation and a trapezoid shape of the tunneling barrier.

$$T(\varepsilon, eV, z) \propto \exp\left(\frac{-2z\sqrt{2m_e}}{\hbar} \sqrt{\frac{\Phi^T + \Phi^S}{2} + \frac{eV}{2} - \varepsilon}\right) \qquad (2.7)$$

The vacuum barrier is determined by the tip and sample work function Φ^T and Φ^S respectively, as well as by the tip-sample distance z. The model includes also the change of the barrier height due to the applied bias voltage V and the electron energy ε. Compared to the theory of Tersoff and Hamann, in the model of Hamer's the sample local density of states is considered at the lateral surface position $(x, y, 0)$ and not at the tip position $\vec{r}^T = (x, y, z)$.

2.2.2 Constant Current Topography

In the constant current mode, a voltage V is applied between tip and sample. The tip height is adjusted so that a constant set point current I_{SP} flows between tip and sample. The tip is scanned laterally (x, y) over the sample line by line using piezo-elements. In the meantime a closed-loop feedback control circuit adjusts the tip height z in such a way that at each point the set point current is reached. In each line the tip displacement is recorded at discrete points, providing a contour $z(x, y)$ of constant current. For small voltages V the area $z(x, y)$ can be interpreted according to Tersoff and Hamann (Eq. 3.9) as a surface of constant local density of states at the Fermi energy. In case of higher voltages, the area $z(x, y)$ has to be interpreted with respect to the model of Hamer as a surface of constant integrated density of states in the interval $[E_F, E_F + eV]$. In both cases, the height profile is a superposition of structural and electronic properties of the sample. For example in a large-scale topography (see Fig. 2.2c) sharp jumps with a height of $\Delta z = 180$ pm, monoatomic steps of the Cu(100) surface, are found which are related to the morphology of the sample.

In this thesis the electronic structure caused by sub-face atoms is of interest. This signature is in general much smaller than a monoatomic step or an adatom on a clean surface. For instance the raw data (only an average plane is subtracted) of a topography measurement (4 nm × 4 nm, 128 pixel × 128 pixel) of two sub-surface iron atoms is shown in Fig. 2.3a. One can see an interference pattern with amplitude of only a few picometers. The local density of states is changed due to the presence of the sub-surface atoms resulting in a standing-wave pattern at the surface. Above areas of reduced electron density in the energy interval
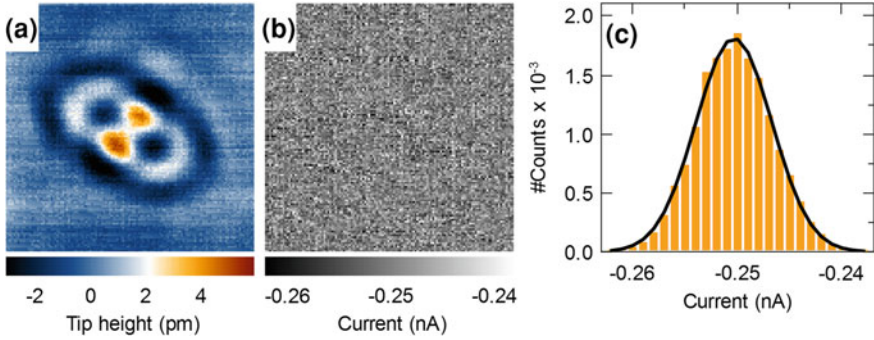
Fig. 2.3 Characterization of the constant current mode. **a** Topography (4 nm × 4 nm, −31 mV, 0.25 nA, raw data) of two sub-surface Fe atoms. The corresponding current measurement is depicted in **b**, as current map and in **c**, as histogram. A Gaussian fit is marked in *black*

$[E_F, E_F + eV]$ the tip has to move closer to the surface. In contrast, the tip is retracted above regions of increased electron density. In order to check the quality and to avoid artifacts of the feedback loop not only the tip displacement but also the current is acquired in the topography mode. If the feedback loop is adjusted, the current map (Fig. 2.3b) shows only a small lateral variation with respect to the set point current I_{SP}. A histogram of the current map Fig. 2.3c reveals a standard deviation of $\sigma = 0.005$ nA which is 2 % of the current set point $I_{SP} = 0.25$ nA.

2.2.3 Multi-bias Topographies

The fastest way to investigate the electronic structure of the sample is to measure topographies of the same area for different applied voltages. If the work function of the sample is laterally constant, changes in the topography can be related to the integral LDOS of the sample. According to Eq. (2.6) the tunneling current is proportional to the integrated local electron density of states $\rho^S(\varepsilon)$ at the surface within $[E_F, E_F + eV]$. This quantity is weighted in the integral by the tip local density of states $\rho^T(\varepsilon)$ and the transmission probability $T(\varepsilon, eV, z)$. As a consequence, states with different energy contribute differently to the tunneling current. For energy intervals where the variation of the electronic properties of the tip and the transmission probability are negligible the measured contour is proportional to the average LDOS.

As the recording of a topography takes some time, it might be possible that the same lateral tip positions are not comparable for different topographies at different bias voltages due to drift effects or tip modifications. To overcome this problem one can use the multi-bias mode. In this mode every scan line is scanned for several tunneling parameter settings (V_n, I_n) before going to the next scan line. This mode provides contours $z_n(x, y)$ which are comparable at the same lateral position (x, y).

2.2.4 dI/dV Spectroscopy

One of the most powerful features of scanning tunneling microscopy is its capability to obtain spectroscopic data with high spatial and energetic resolution. Scanning tunneling spectroscopy (STS) provides information about the LDOS of the sample as function of the lateral position (x, y) and a certain energy ε. The LDOS can be approximately derived from the differential conductance $dI/dV(V)$ at a certain bias voltage V. Since the main results presented in this thesis are obtained by spectroscopic measurements, the description of this technique and its interpretation will be discussed in detail in the following section.

Taking the tunneling current expressed by Eq. (2.6) and using Leibnitz's rule, the derivative of the current gives three terms

$$
\begin{aligned}
\frac{dI}{dV}(V, x, y, z) \propto\ & \rho^S(x, y, eV)\rho^T(0)T(eV, V, z) \\
& + \int_0^{eV} d\varepsilon \rho^S(x, y, \varepsilon)\rho^T(\varepsilon - eV)\frac{dT(\varepsilon, V, z)}{dV} \\
& + \int_0^{eV} d\varepsilon \rho^S(x, y, \varepsilon)T(\varepsilon, V, z)\frac{d\rho^T(\varepsilon - eV)}{dV}
\end{aligned}
\tag{2.8}
$$

While this equation is quite complicated, it can be simplified assuming a constant LDOS of the tip ($\rho^T = $ const) and a constant transition probability ($T(\varepsilon, V, z) = $ const). These assumptions are valid for small energies, i.e. ε is small compared to the work functions of tip and sample and $\rho^T(\varepsilon)$ is featureless compared to $\rho^S(\varepsilon)$. With these assumptions the second and the third term vanish and the derivative becomes

$$
\frac{dI}{dV}(V, x, y) \propto \rho^S(x, y, eV)
\tag{2.9}
$$

For the investigation of sub-surface atoms the change of the LDOS $\Delta\rho^S(x, y, \varepsilon)$ due to the presence of the impurity in comparison to the unperturbed surface is of interest. This quantity can be obtained by measuring a reference spectrum of the free unperturbed surface $dI_0/dV(V)$ far away from the impurity. The background subtracted differential conductance $\Delta dI/dV(V)$

$$
\frac{\Delta dI}{dV} = \frac{dI}{dV}(x, y, V) - \frac{dI_0}{dV}(V) \propto \Delta\rho^S(x, y, eV)
\tag{2.10}
$$

is proportional to the change in the LDOS at the position (x, y) in comparison to the unperturbed surface [18].

Technically, the tip is placed over an area of interest with a defined distance to the sample given by the stabilizing tunneling parameters (V_{SP}, I_{SP}). Then the feedback loop is temporarily switched off and a spectrum is recorded within a certain voltage

range. After that, the feedback loop is reactivated and the tip moves to the next scan point. Experimentally, there are several possibilities to measure the differential conductance. One approach is to record an $I(V)$-curve at every scanning point. By using further data processing including averaging and numerical differentiation this provides a complete map of the differential conductance $dI/dV(x, y, V)$ as a function of lateral tip position (x, y). Although the numerical approach is simple, the obtained spectroscopic data is usually very noisy. Because of this one has to average over a long time to obtain reasonable data. To get high resolution spectra on shorter time scales a lock-in technique has been developed and implemented into the existing system. The basic idea rest upon the observation that the noise of the tunneling current is not determined by white noise but rather by 1/f noise. The advantage of the lock-in technique is to measure the first derivative directly and to shift the signal from zero frequency (as it is the case for the numerical derivative) with a high noise level towards higher frequencies with a lower noise level.

2.2.5 Lock-in Technique

A lock-in method was implemented to obtain spectroscopic data with high signal to noise ratio. In order to control all necessary parameters of this technique and to integrate the lock-in amplifier into the existing electronic setup a digital signal processing (DSP) board (ADwin-light-16 by Jäger, Lorsch) is used.[2] Details of the programming and technical aspects can be found in [19]. In Fig. 2.4 the general scheme of the electronic setup is shown. A small sinusoidal voltage $V_m \sin(\omega_m t)$ with amplitude V_m and frequency ω_m, generated by the lock-in is added to the applied bias voltage V. After the I/V-converter, the signal is split into a direct (DC) and an alternating (AC) signal using a low pass and a band pass, respectively. The DC part enters the feedback control which is carried out by a second DSP-board and the AC signal is amplified and measured by the lock-in amplifier.

2.2.6 Basic Principle

In the following, the main concept and advantages of the lock-in technique will be introduced. The basic idea is to modulate the tunneling voltage. A sketch of the time dependent voltage V is shown in Fig. 2.5a.
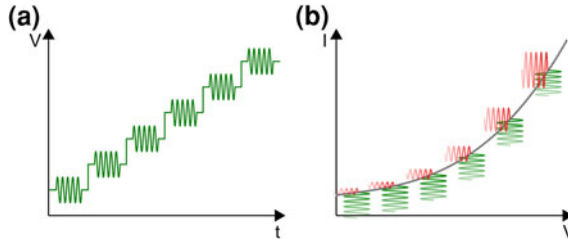
The voltage modulation results in an alternating current (AC) signal. The amplitude of the current oscillation is directly connected to the slope of the $I(V)$-curve, see Fig. 2.5b. Using the model of Tersoff and Hamann the tunneling current is given by the following formula

---

[2] An identical board takes care of the z–piezo displacement and realizes the feedback loop.
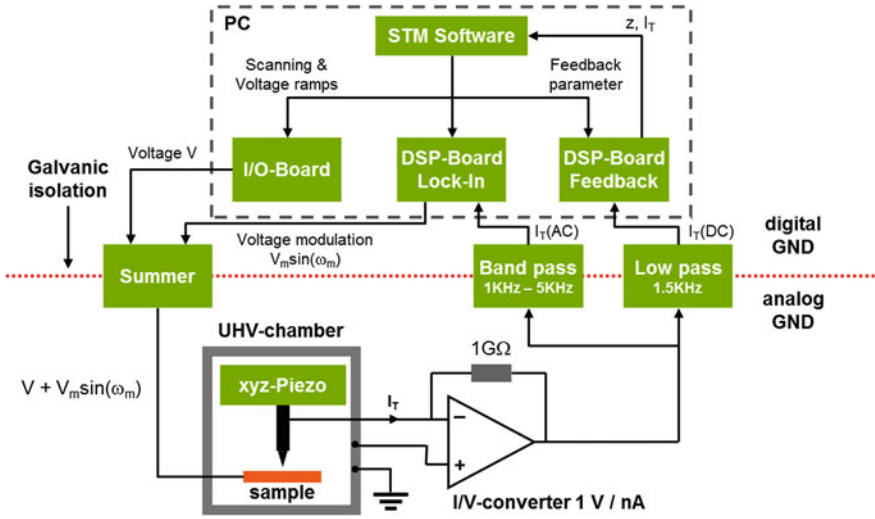
Fig. 2.4 Implementation of the digital lock-in technique into the electronic setup. The digital lock-in is realized by a digital signal processor (DSP) board. The modulation is added to the bias voltage and applied to the sample. Afterwards, the signal is split into a direct current (DC) and an alternating (AC) going to the feedback control and to the lock-in

Fig. 2.5 Scheme of the lock-in technique. **a** The tunneling voltage is modulated by a sinusoidal voltage. **b** The voltage modulation leads to an alternating current signal. The amplitude of the alternating current can be connected to the first derivative of the $I(V)$-curve

$$I \propto \int_{0}^{eV+V_m \sin(\omega_m t)} \rho^S(\varepsilon) d\varepsilon \qquad (2.11)$$

Expanding the current in a Taylor series (around $t = 0$) yields

$$I(t) \propto \sum_{n=0}^{\infty} \frac{(V_m)^n}{n!} I^{(n)}(V) \sin^n(\omega_m t) \qquad (2.12)$$

where $I^{(n)}(V)$ is an abbreviation for the n-th derivative of the current I at the voltage V. By using an algebraic identity for the sine function one obtains directly the Fourier series of the current.

$$I(t) \propto \sum_{n=0}^{\infty} \frac{(V_m)^n}{n!} I^{(n)}(V) \sum_{k=0}^{n} \frac{1}{2^n} \binom{n}{k} \cos\left[(n-2k)\left(\omega_m t - \frac{\pi}{2}\right)\right]$$
$$= \sum_{n=0}^{\infty} A_n \sin(n\omega_m t + \phi_n)$$
(2.13)

Typically, the Fourier spectrum of the current will have only a few harmonics of non-negligible amplitude A_n. The direct current part, the A_0 term, has normally the highest magnitude of all frequencies. For the alternating current ($A_{n>0}$) usually only the amplitude A_1 of the fundamental frequency ω_m is significant. The amplitude of all higher frequencies is comparatively small. This approximation is justified in cases where the $I(V)$-curve nearly shows a linear behavior in the voltage range $[V - V_m; V + V_m]$.

The amplitude of the modulation frequency A_1 has various contributions. Explicitly, up to the fifth order, these terms are

$$A_1 = V_m I^{(1)}(V) + \frac{1}{8}(V_m)^3 I^{(3)}(V) + \frac{1}{96}(V_m)^5 I^{(5)}(V) + \cdots$$
(2.14)

Within the same argument as before, the linear dependency of the $I(V)$-curve in the considered voltage interval, the amplitude A_1 of the current modulation with frequency ω_m is proportional to the first derivative of the $I(V)$-curve and therefore to the LDOS of the sample.

The first derivative of the $I(V)$-curve can then be calculated by the normalized integral over time $\tau \gg 2\pi\omega_m^{-1}$ of the alternating current signal multiplied by a reference signal

$$\frac{dI}{dV}(V) = \frac{2}{V_m \tau} \int_0^{\tau} \underbrace{\sin(\omega_m t + \varphi)}_{Reference} I(t) dt$$
(2.15)

The reference signal is taken directly from the modulation generator and is phase shifted by φ. This phase shift is important since the alternating current signal is not in phase with the voltage modulation due to electronic components and filters. Another important aspect is the capacitance C resulting from the connecting wires and the tip-sample geometry. This capacitance gives rise to an alternating current I_c which is independent of the tunneling current I_t. Due to the capacitance the current is phase shifted by 90° compared to the tunneling current which behaves like an ohmic resistor. The amplitude of this parasitic current can be of the same order of magnitude or even higher than the signal of interest. For example a capacitance of $C = 0.8\,\text{pF}$ and a modulation frequency of $f_m = 2,000\,\text{Hz}$ lead to an impedance

of $X_c = (2\pi f_m C)^{-1} = 100\,\text{M}\Omega$. Using a voltage modulation of $V_m = 1\,\text{mV}$ this results in a parasitic alternating current $I_c = V_m X_c^{-1} = 10\,\text{pA}$. Considering a tunnel resistance of $R_T = 1\,\text{G}\Omega$ and the same voltage modulation V_m the signal of interest $V_m R_T^{-1} = 1\,\text{pA}$ is one order of magnitude smaller than I_c. In order to obtain spectroscopic data of good quality under such conditions, the phase of the reference signal has to be adjusted correctly. To achieve this goal in the experiment the tip is retracted ($R_T = \infty$) and the phase of the reference is adjusted that the above integral in Eq. (2.15) vanishes.

So far an ideal system without noise is considered. In reality the noise determines the averaging time τ in Eq. (2.15) to obtain the intended quality. For long averaging times $\tau\omega_m/2\pi \rightarrow \infty$ only the input signal from the tunneling resistance survives. All other signatures which are not phase correlated or have a different frequency than the reference signal vanish. Considering only white noise the indirect numerical derivative and the direct lock-in signal have the same signal to noise ratio for same bandwidth and averaging times. In the case of a tunneling junction it turns out that the noise is not white but rather shows a 1/f characteristic (Schottky noise) [20, 21] and contains also system specific parasitic signals (e.g. stemming from vibrational modes). The advantage of the lock-in amplifier is to measure the first derivative directly and to shift the signal from zero frequency (as it is the case for the numerical derivative) towards the modulation frequency f_m. Using a modulation frequency which has a low noise level, therefore allows increasing the signal to noise ratio. So far the signal quality was discussed only for nearly infinite averaging times τ which are not realized in any experiment. If the averaging time τ is finite, the signal has not only contributions of the reference frequency but also components with slightly higher or lower frequencies. Since the noise of the tunnel junction shows 1/f behavior, the signal to noise ratio of a lock-in is still better compared to the numerical derivation which acquires the data around zero frequency.

2.2.7 Data Processing

For a quantitative comparison of the experimental data with theory one has to take care of the STM calibration. Inaccuracies of the piezo constants and a small mis-angle of x- and y-scan axis lead to a distorted image of the crystal surface. The measured data can be calibrated by taking atomic resolved topographies as a reference. As atomic resolution was achieved at least once in every experiment presented in this thesis the information of the crystallographic directions for each sample is provided. Raw data obtained on a clean Cu(100) surface (see Fig. 2.6a) reveals a sheared and stretched surface unit cell. The atomic resolved data as well as the peak position of the Fourier transformed data can be used to calculate a 2×2 Matrix to calibrate the raw data. The calibrated images are oriented with the
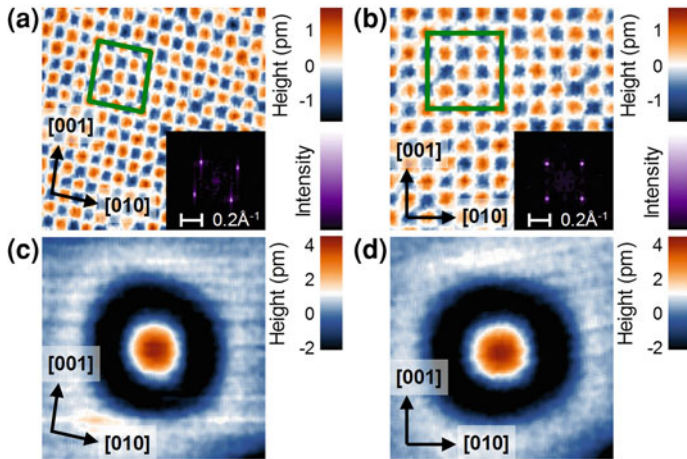
Fig. 2.6 Calibration of the measured STM data. **a** Atomically resolved topography (3 nm × 3 nm, −10 mV and 1 nA) of a clean Cu(100) surface. The corresponding powerspectrum is depicted in the *inset*. A 2 × 2 supercell of the obeserved surface unit cell is highlighted in *green*. Both the atomic corrugation as well as the peaks in the powerspectrum can be used to calibrate the measurement. **b** Calibrated topography (2.2 nm × 2.2 nm) and powerspectrum clearly showing the cubic surface unit cell of Cu(100). Again a 2 × 2 supercell is highlighted in *green*. **c** Standing-wave interference pattern of an embedded Fe impurity (2.0 nm × 2.0 nm, 10 mV and 1 nA). **d** Calibrated topography of the Fe atom (1.8 nm × 1.8 nm)

x-axis parallel to the [010] crystallographic direction. The successful data processing, indicating a cubic surface unit cell, is shown in Fig. 2.6b.

Since the sample is a single crystal, the crystallographic directions are equal for all lateral positions on the sample surface. The same shear and stretch matrix can be applied also to non-atomically resolved topographies (see Fig. 2.6c, d). The above described procedure has been applied to all data sets presented in this thesis. For most of the data sets the x- and y-axis of the topography are aligned to the [010] and [001] crystallographic direction, respectively. For the case that the crystal direction will point in other directions the coordinate system is given. When no explicit coordinate system is given in a topography the above convention for the x- and y-axis holds on.

2.2.8 STS Normalization

In order to gain and compare spectroscopic information from a *dI/dV*-map one has to take the tip-sample distance into consideration. Since the electronic properties of the sample are locally changed due to the presence of an impurity the tip-sample

distance might not be the same for all lateral positions (x, y). If the tip is stabilized in constant current mode (topography mode), the tip height is adjusted to obtain the set-point current I_{SP} at a chosen bias voltage V_{SP}. Moreover, if thermo voltages are neglected, the current I has to vanish at $V = 0$. These two boundary conditions $I(V_{SP}, x, y) = I_{SP}$ and $I(V = 0, x, y) = 0$ restrict the variation of the dI/dV signal to the interval $V \in [V_{SP}, 0]$. For the inverse set point voltage $V = -V_{SP}$ no boundary condition exists. Therefore, the *dI/dV*-curve shows particularly strong variations on this side ($V \in [0, -V_{SP}]$). The missing information on the side of the set point voltage V_{SP} is compensated by the tip-sample distance z. This artifact can be successfully removed by normalizing the spectroscopy data to a constant tip-sample distance z^*. This method, the so-called topographic normalization, was first proposed by Garleff et al. in 2004 [22].[3]

The topographic normalization rests upon the assumption that the tunnel current depends exponentially on the tip-sample distance. The normalized spectrum can be directly obtained using the Hamer's model

$$\frac{dI}{dV}(V, x, y)\bigg|_{z=z^*} = \frac{dI}{dV}(V, x, y) \cdot \exp(2\kappa[z(x, y) - z^*]) \qquad (2.16)$$

where κ is defined by the following relation

$$\kappa = \sqrt{\frac{2m_e \Phi}{\hbar^2}} \qquad (2.17)$$

Here $\Phi = (\Phi^T + \Phi^S)/2$ is the mean value of tip Φ^T and sample Φ^S work function. For the calculation of κ it is assumed that the energy dependence of the transmission coefficient can be neglected for small energies and the work function Φ does not depend on the lateral position of the tip. As reference distance z^* usually the tip-sample distance of the free surface far away from an impurity is used. Due to the topographic normalization spectra of different lateral positions are comparable.

In this work a mean value of tip Φ^T and sample Φ^S work function of $\Phi = 4.2\,\mathrm{eV}$ is used. This value is in good agreement with literature values for the work function of the pure Cu(100) surface ($\Phi^S = 4.59\,\mathrm{eV}$) and of polycrystalline tungsten ($\Phi^T = 4.55\,\mathrm{eV}$) [24]. Moreover, measurements of the tip-sample distance as function of the set point current give a similar value for the mean barrier height ($\Phi = 4.27\,\mathrm{eV}$) [6].

---

[3] An identical formalism was introduced before by Feenstra [23]. In this paper he considered a tip movement towards the surface while acquiring STS data at *one* lateral tip position.

References

1. Quaas N (2003) Scanning tunnelling microscopy of co-impuried noble metal surfaces: Kondo-effect, electronic surface states and diffusional atom transport. Ph. D. thesis, Georg-August-Universität zu Göttingen

2. Weismann A (2003) Rastertunnelspektroskopie auf magnetisch verunreinigten Cu- und Ag-Einkristalloberflächen. Diploma thesis, Georg-August-Universität zu Göttingen

3. McGuire GE (1979) Auger electron spectroscopy reference manual. Plenum, New York

4. Weismann A (2008) Scanning tunneling spectroscopy on subsurface magnetic atoms in copper: electron focusing and Kondo effect. Ph. D. thesis, Georg-August-Universität zu Göttingen

5. Kloth P (2010) Quantentopfzustände in metallischen Heterostrukturen. Diploma thesis, Georg-August-Universität zu Göttingen

6. Prüser H (2008) Rastertunnelspektroskopie an magnetischen Atomen: Kondo-Effekt von Eisen und Kobalt in Kupfer. Diploma thesis, Georg-August-Universität zu Göttingen

7. Binnig G, Rohrer H, Gerber C, Weibel E (1982) Phys Rev Lett 49:57

8. Binnig G, Rohrer H, Gerber C, Weibel E (1983) Phys Rev Lett 50:120

9. Bonnell D (2001) Scanning probe microscopy and spectroscopy, 2nd edn. Wiley-VCH, New York

10. Chen CJ (1993) Introduction to scanning tunneling microscopy. Oxford University, USA

11. Blügel S (2010) Theorie der Rastertunnelmikroskopie. Script

12. Besocke K (1987) Surf Sci 181:145

13. Druga T (2014) Graphen auf Siliziumcarbid: elektronische Eigenschaften und Ladungstransport. Ph. D. thesis, Georg-August-Universität zu Göttingen

14. Bardeen J (1961) Phys Rev Lett 6:57

15. Tersoff J, Hamann DR (1983) Phys Rev Lett 50:1998

16. Tersoff J, Hamann DR (1985) Phys Rev B 31:805

17. Hamers RJ (1989) Annu Rev Phys Chem 40:531

18. Wahl P, Diekhöner L, Schneider MA, Kern K (2008) Rev Sci Instrum 79:043104

19. Eggebrecht T (2010) Entwicklung eines Lock-In-Verfahrens zur hochauflösenden Rastertunnelspektroskopie. Bachelor thesis, Georg-August-Universität zu Göttingen

20. Möller R, Esslinger A, Koslowski B (1990) J Vac Sci Tech A: Vac Surf Films 8:590

21. Koslowski B (1996) AIP Conf Proc 371:149

22. Garleff JK, Wenderoth M, Sauthoff K, Ulbrich RG, Rohlfing M (2004) Phys Rev B 70:245424

23. Feenstra RM (1994) Phys Rev B 50:4561

24. Stöcker H (2000) Taschenbuch der Physik. Harry Deutsch, Thun

Scanning Tunneling Spectroscopy of Magnetic Bulk Impurities
From a Single Kondo Atom Towards a Coupled System
Prüser, H.